www.MaterialsViews.com

ADVANCED
ENERGY
MATERIALS
www.advenergymat.de

FULL PAPER

Layer-by-Layer Na$_3$V$_2$(PO$_4$)$_3$ Embedded in Reduced Graphene Oxide as Superior Rate and Ultralong-Life Sodium-Ion Battery Cathode

Yanan Xu, Qiulong Wei, Chang Xu, Qidong Li, Qinyou An,* Pengfei Zhang, Jinzhi Sheng, Liang Zhou, and Liqiang Mai*

Na$_3$V$_2$(PO$_4$)$_3$ (NVP) is regarded as a promising cathode for advanced sodium-ion batteries (SIBs) due to its high theoretical capacity and stable sodium (Na) super ion conductor (NASICON) structure. However, strongly impeded by its low electronic conductivity, the general NVP delivers undesirable rate capacity and fails to meet the demands for quick charge. Herein, a novel and facile synthesis of layer-by-layer NVP@reduced graphene oxide (rGO) nanocomposite is presented through modifying the surface charge of NVP gel precursor. The well-designed layered NVP@rGO with confined NVP nanocrystal in between rGO layers offers high electronic and ionic conductivity as well as stable structure. The NVP@rGO nanocomposite with merely ≈3.0 wt% rGO and 0.5 wt% amorphous carbon, yet exhibits extraordinary electrochemical performance: a high capacity (118 mA h g^{-1} at 0.5 C attaining the theoretical value), a superior rate capability (73 mA h g^{-1} at 100 C and even up to 41 mA h g^{-1} at 200 C), ultralong cyclability (70.0% capacity retention after 15 000 cycles at 50 C), and stable cycling performance and excellent rate capability at both low and high operating temperatures. The proposed method and designed layer-by-layer active nanocrystal@rGO strategy provide a new avenue to create nanostructures for advanced energy storage applications.

1. Introduction

The development of energy storage systems with green chemistry, high efficiency, long life, high safety, and low cost is one of the biggest challenges faced by human society.[1–4] Throughout the current energy storage technologies, the battery systems represent one of the most promising candidates with high energy efficiency for large-scale smart grid energy storage systems (ESSs). Lithium-ion batteries (LIBs) are an option.[5–11]

Y. N. Xu, Q. L. Wei, C. Xu, Q. D. Li, Prof. Q. Y. An,
P. F. Zhang, J. Z. Sheng, Prof. L. Zhou,
Prof. L. Q. Mai
State Key Laboratory of Advanced Technology
for Materials Synthesis and Processing
Wuhan University of Technology
Hubei, Wuhan 430070, P. R. China
E-mail: anqinyou86@whut.edu.cn; mlq518@whut.edu.cn

However, the limited lithium resource in earth is detrimental to the further application due to the possible increasing cost and unstable energy supply.[12–15] Therefore, there is an urgent demand for developing alternative energy storage devices with low cost while maintaining a comparable performance to LIBs. Among them, sodium-ion batteries (SIBs) have become the worldwide focus owing to abundant resources and low cost.[16–19] To develop high-performance SIBs, it remains challenging to discover/develop suitable electrode materials (especially cathode) to satisfy the requirement of long-term cycling stability and rate-capability.

Owing to larger radius of Na$^+$ than that of Li$^+$ (0.98 vs 0.69 Å), various cathode materials with large open frameworks, including layered transition-metal oxides[19–25] and polyanionic compounds,[2,13,18,26–33] have been developed for (1) the improved sodium storage capacity, (2) the facilitated Na$^+$ diffusion in the lattice, and (3) the restricted structure degradation caused by Na$^+$ insertion/extraction. The NASICON (sodium (Na) super ion conductor) Na$_x$M$_2$(NO$_4$)$_3$ (M = transition metal, N = P^{5+}, Si^{4+}, S^{6+}, and Mo^{6+}) structure with 3D large open framework allows for rapid and reversible ion diffusion in the lattice, which is now developed as electrode with promising electrochemical performance.[34] Among these, the Na$_3$V$_2$(PO$_4$)$_3$ (NVP) becomes a "shining star" with high sodium diffusion ability and remarkable high energy density (i.e., 400 Wh kg^{-1}).[18] However, the high ionic diffusion ability of NVP is accompanied with poor electronic conductivity,[35] which results in the low utilization of active materials even at low rates. In order to obtain remarkable performance of NVP, the hurdles of poor rate capability and cycling stability need to be further addressed. Recently, carbon-coated active nanocrystals embedded in a porous carbon matrix, which demonstrated excellent rate performance and cycling stability for Li$_3$V$_2$(PO$_4$)$_3$ cathodes,[36,37] as well as for NVP cathodes.[38–40] In general, the porous carbon content is usually high, which may lead to the decrease of tap density and entire cell volumetric energy density.[41,42] Li and co-workers reported adaptive graphene gel films as a highly compact electrode with

ADVANCED
ENERGY
MATERIALS
www.advenergymat.de

Materials
Views
www.MaterialsViews.com

continuous ion and electron transport network.[43] Such layer-by-layer structure delivered superior rate performance with high packing density. Considering the advantages of graphene for improving the electrochemical performance and the intrinsic NASICON structure of NVP,[44–48] the construction of layer-by-layer systems composed of graphene and NVP sheets will be an acceptable attempt, which exhibit improved electrochemical performance. Relative research has rarely been reported.

Herein, for the first time, we developed a novel, straightforward and self-assembly approach for the fabrication of layer-by-layer structured NVP@reduced graphene oxide (NVP@rGO) nanocomposites based on the interfacial coupling of graphene oxide nanosheets (GO-NSs) and NVP/acetylacetone (acac) gel. Through the hydrogen bonds and amphiphilic interactions between the GO-NSs and NVP/acac gel, the NVP/acac gel uniformly and stably disperse in the GO matrix. After freeze-drying and annealing, GO is reduced to rGO in the reducing atmosphere to obtain the layer-by-layer structured NVP@rGO composite. The rGO matrices provide facile and rapid electron transport while the stable NASICON structure of NVP offers superior ion diffusion ability. The resulted electrochemical performance of the NVP@rGO nanocomposite is impressive: a remarkable high-rate capacity of 41 mA h g^{-1} (35% of the full capacity) at 200 C (22 A g^{-1}), in which the discharge process can be completed in only 6.7 s. A long cycling life with capacity retention of 70% after 15 000 cycles demonstrates the stable structure of our designed layered composites. Furthermore, our designed NVP@rGO nanocomposite also displays stable cycling performance and excellent rate capability at both low and high operating temperatures.

2. Results and Discussion

A schematic depiction of the synthesis process is displayed in **Figure 1**. The detailed synthesis processes are described in the Experimental Section. Briefly, the Na_2CO_3, $V(C_5H_7O_2)_3$ ($V(acac)_3$), $NH_4H_2PO_4$ are directly dissolved in deionized water to obtain a light blue solution (Figure S1a, Supporting Information). Tyndall effect is not obvious, which demonstrates that the dispersion is not a colloidal suspension. In a typical process (Figure 1a), the GO-NSs/water dispersions are directly added into the light blue solution with continuous stirring. However, the GO-NSs rapidly self-aggregate and agglomerate (Figure S1b, Supporting Information) and are hardly redispersed even after ultrasonication. Then the heterogeneous NVP/GO mixed precursor is obtained after freeze-drying (Figure S2a,b, Supporting Information). After annealing in H_2/Ar (5/95 in vol.), the inhomogeneous NVP-particles and rGO-NSs composites (denoted as NVP-P/rGO) are obtained. It is noted that the self-aggregate of rGO in the composite is not beneficial for supporting highly electronic conductivity. To avoid the agglomeration of the GO-NSs and re-construct a more effective structure, a modified approach is undertaken as schematically illustrated in Figure 1b. Through a hydrothermal treatment of the light blue solution, a jelly-like gel with an obvious Tyndall effect (Figure S1c, Supporting Information) is obtained, demonstrating a colloidal system. The Zeta potential, which is an important factor for characterizing the stability of colloidal dispersions, is further measured. Generally, particles with zeta potentials >30 mV or <−30 mV are considered as stable dispersions due to their inter-particle electrostatic repulsion.[49,50] The Zeta potential of the NVP gel is −48.6 mV (Table S1, Supporting Information), indicating stable dispersions of colloids. The as-synthesized GO-NSs exhibit an average Zeta potential of −36.6 mV in aqueous solution. After vigorously mixing the gel with GO-NSs dispersions (Figure S1d, Supporting Information), the homogeneous mixed gel still shows obvious Tyndall effect (Figure S1d, Supporting Information) with a Zeta potential stable at −45.3 mV. The mixed dispersion can be stable for more than one week. For the GO-NSs, the abundant functional groups provide noncovalent
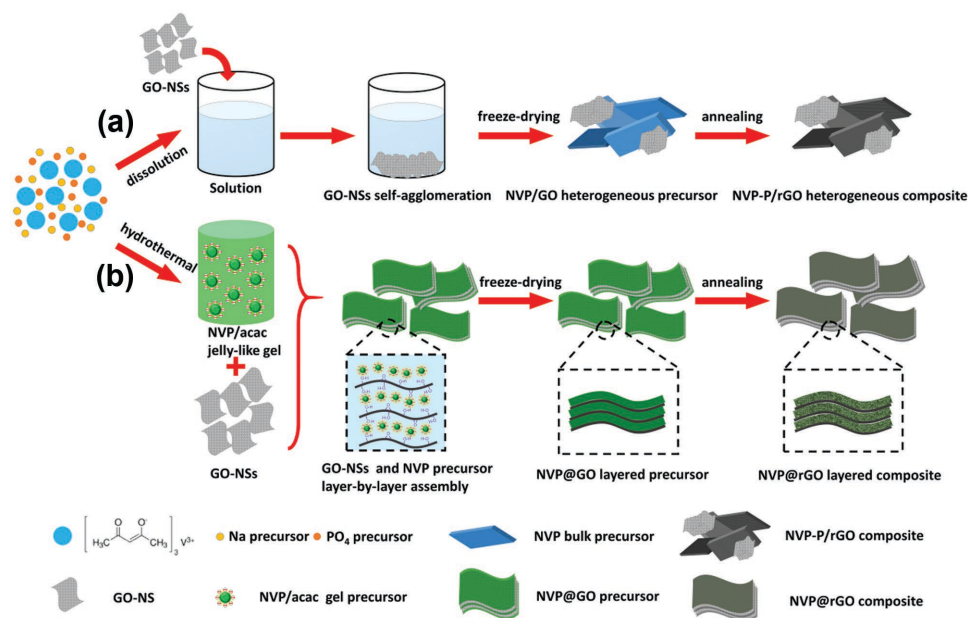

Figure 1. Schematic illustration for the synthesis of a) NVP-P/GO and b) NVP@rGO composites.

Materials Views
www.MaterialsViews.com

ADVANCED
ENERGY
MATERIALS
www.advenergymat.de

FULL PAPER

forces including hydrogen bonding, amphiphilic and electrostatic interactions.[49] Owing to (1) the hydrogen bonding and electrostatic interactions among the GO-NSs and NVP colloids in the aqueous solution and (2) the viscosity of the jelly-like gel NVP precursor, the self-aggregation/agglomeration of GO-NSs is largely inhibited. Meanwhile, the GO-NSs homogeneously disperse in the mixed gel with uniform coating of NVP precursor. In order to duplicate the layered structure of GO-NSs, a freeze-drying approach is employed, as shown in the scanning electron microscopy (SEM) images in Figure S3a,b of the Supporting Information. After annealing, the space-confined growth of NVP precursor in between the rGO layers results in well interconnected NVP@rGO layer-by-layer structure. As a control experiment, direct freezing-drying and annealing of NVP gel result in the formation of NVP/C-particles (denoted as NVP-P/C).

Figure 2a shows the X-ray diffraction (XRD) patterns of the NVP-P/C, NVP-P/rGO, and NVP@rGO. All of the diffraction peaks are indexed to the rhombohedral NVP structure (JCPDS No. 53-0018),[18] indicating a high purity. Rietveld refinements of XRD patterns for the three samples were performed, as shown in Figure S4 of the Supporting Information. All peaks in the XRD patterns are indexed to NASICON structure with R-3c space group. The lattice parameters for the three samples (Table S2, Supporting Information) compare well with the standard phase, indicating the good crystal structure of the obtained samples. Comparing the lattice parameters of three samples, the lattice parameters of NVP@rGO are the smallest, suggesting a more stable structure closed to the standard NASICON phase, which will be beneficial for the cycling performance. Determined from CHN elemental analysis, the carbon contents of NVP-P/C, NVP-P/rGO, and NVP@rGO are only 0.57 wt%,

3.79 wt%, and 3.50 wt%, respectively, which indicates that the rGO content of NVP@rGO is ≈3.0 wt%. The low carbon contents of the as-synthesized samples were also confirmed by TGA (Figure S5, Supporting Information). The NVP@rGO possesses lower carbon content than NVP-P/rGO. This is because the decomposition of organics during the pretreatment of hydrothermal process leads to the decreased carbon content in the finial products. Raman spectra of the three samples are shown in Figure 2b–d. The D (disorder-induced phonon mode) and G (graphite band) bands are observed at around 1340 and 1580 cm^{-1}, respectively.[48] The intensity ratios of D band to G band (I_D/I_G) for NVP-P/C, NVP-P/rGO, and NVP@rGO are around 1.41, 1.32, and 1.20, respectively. The existence of organics (acac) in the synthesis process of NVP will result in the formation of amorphous carbon in the final products. Thus, the decreased amorphous carbon content and predecomposition process may result in the slight higher graphitization degree in NVP@rGO than that in NVP-P/rGO. In addition, based on Gaussian numerical simulation, the two broad peaks of each sample can be decomposed into four peaks.[51,52] The peaks around 1350 cm^{-1} (2) and 1590 cm^{-1} (4) are correlated to sp^2-type carbon (graphitized carbon), while the other two peaks around 1180 cm^{-1} (1) and 1510 cm^{-1} (3) are relevant to sp^3-type carbon (amorphous carbon and the defects). A low integrated area ratio of sp^3 to sp^2 (A_{sp}^3/A_{sp}^2) indicates that a large fraction of carbon exists as the sp^2-type. The fitted A_{sp}^3/A_{sp}^2 values of the NVP-P/C, NVP-P/rGO, and NVP@rGO are 0.296, 0.163, and 0.161, respectively, suggesting the highest content of sp^2-type carbon of NVP@rGO.[51,52]

Figure 3a shows that the NVP@rGO is sheet-like structure with tens of micrometers, which is due to the ice template effect
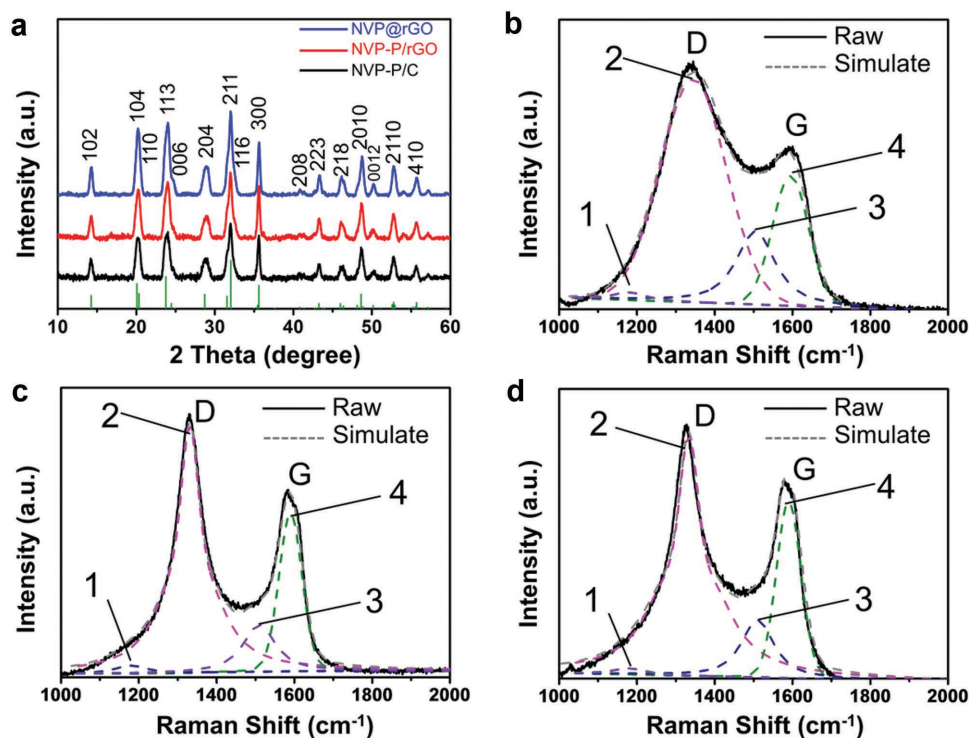

Figure 2. a) XRD patterns of the samples. Raman spectra of the b) NVP-P/C, c) NVP-P/rGO, and d) NVP@rGO.
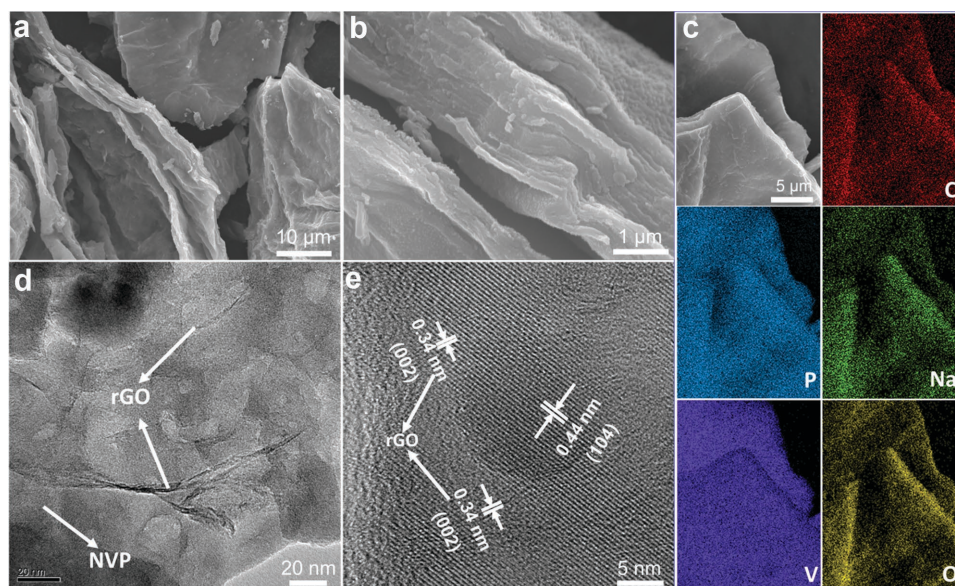
FULL PAPER

Figure 3. a,b) SEM images, c) elemental mapping images, d) TEM image, and e) HRTEM image of the NVP@rGO.

during the freeze-drying process. SEM image (Figure 3b) clearly displays the sheets are composed by multistacked layers. The elemental mappings display the existence and uniform distribution of C, P, Na, V, and O in the NVP@rGO composite (Figure 3c). Moreover, the transmission electron microscopy (TEM) images (Figure S6, Supporting Information and Figure 3d) prove the layer-by-layer assembly of NVP@rGO composite, consisting of NVP nanocrystal in between rGO. The high-resolution TEM (HRTEM) image (Figure 3e) clearly displays lattice fringes with a *d*-spacing of 0.44 nm, corresponding to the (104) planes of the rhombohedral NVP.[38] In addition, a *d*-spacing of 0.34 nm corresponding to the (002) planes of the multilayer graphene is also clearly observed.[53] To further investigate the structure of NVP@rGO, the NVP@rGO composites are dipped in hydrofluoric acid to remove the NVP crystals.[36,37] The rGO nanosheets with stack-layered morphology is largely retained (Figure S7, Supporting Information). In order to investigate the effect of freeze-drying process, the morphologies of the NVP@rGO material prepared without freeze-drying treatment (named unlayered-NVP@rGO) are shown in Figure S8 of the Supporting Information. The SEM images show that rGO sheets separate from the agminated NVP particles, which is because the coagulation of the mixed gel precursors in the directly normal drying and followed annealing process leads to the uneven dispersion of rGO and NVP particles. For the NVP-P/C (Figure S9a, Supporting Information), it is consisted of NVP nanoparticles with uniform size of ≈200 nm forming connected structure. The TEM image (Figure S9b, Supporting Information) shows that there are pores among the NVP particles. In the case of NVP-P/rGO (Figure S9c–e, Supporting Information), it can be observed that agglomerated NVP bulk particles are separated from restacked graphene sheets. In addition, packing density is an important factor of the electrode materials, which have close relationship with their morphology. Figure S10 of the Supporting Information shows the volume occupied comparison of NVP-P/C, NVP-P/rGO,

and NVP@rGO with the same mass. The volume ratio of NVP@rGO:NVP-P/rGO:NVP-P/C is 1:1.07:1.29, indicating the improved packing density of NVP@rGO among the three samples. From the above results, it can be concluded that the layer-by-layer NVP@rGO composite has the intimate contact between the active NVP and conductive rGO matrix. It is expected that this structure not only improves the electrical conductivity of the entity, but also suppresses the agglomeration of NVP nanocrystals during the electrochemical reaction process, providing improved activity and stability.

Further investigations of the electrochemical performances for the prepared samples were carried out by the assembly of half-cells (2016-type coin cell) with metallic sodium as anode. The charge and discharge profiles of the samples at 1 C (1 C = 110 mA g^{-1}) in 2.5–4.0 V are shown in **Figure 4**a and Figure S11a of the Supporting Information. All the samples have coupled flat charge and discharge plateaus at around 3.4 V, corresponding to the redox pair of V^{3+}/V^{4+}.[2,18,38,39] The designed NVP@rGO composite delivers the smallest overpotential (56 mV) and highest capacity of 117 mA h g^{-1} when compared to those of the NVP-P/C (189 mV and 80 mA h g^{-1}), NVP-P/rGO (180 mV and 87 mA h g^{-1}) and unlayered-NVP@rGO (80 mV and 105 mA h g^{-1}). After 100 cycles (Figure 4b and Figure S11b, Supporting Information), the capacity retention of NVP@rGO is 98.0%, which is higher than that of NVP-P/C (85.5%), NVP-P/GO (91.9%) and unlayered-NVP@rGO (94.0%). Figure 4c shows the rate performance (corresponding charge–discharge curves shown in Figure S12, Supporting Information) of NVP@rGO, while the rates range from 0.5 to 200 C. At the initial low rate of 0.5 C, the NVP@rGO delivers a high discharge capacity of 118 mA h g^{-1}. With the current rate is increased to 1, 2, 5, and 10 C, the discharge capacities still remain 115, 112, 109, and 107 mA h g^{-1}, respectively. Even at the high rate of 50 and 100 C, a reversible capacity of 91 and 73 mA h g^{-1} is achieved, corresponding to 77% and 62% of the capacity obtained at 0.5 C. The corresponding charge/discharge time is 60 and 24 s for 50
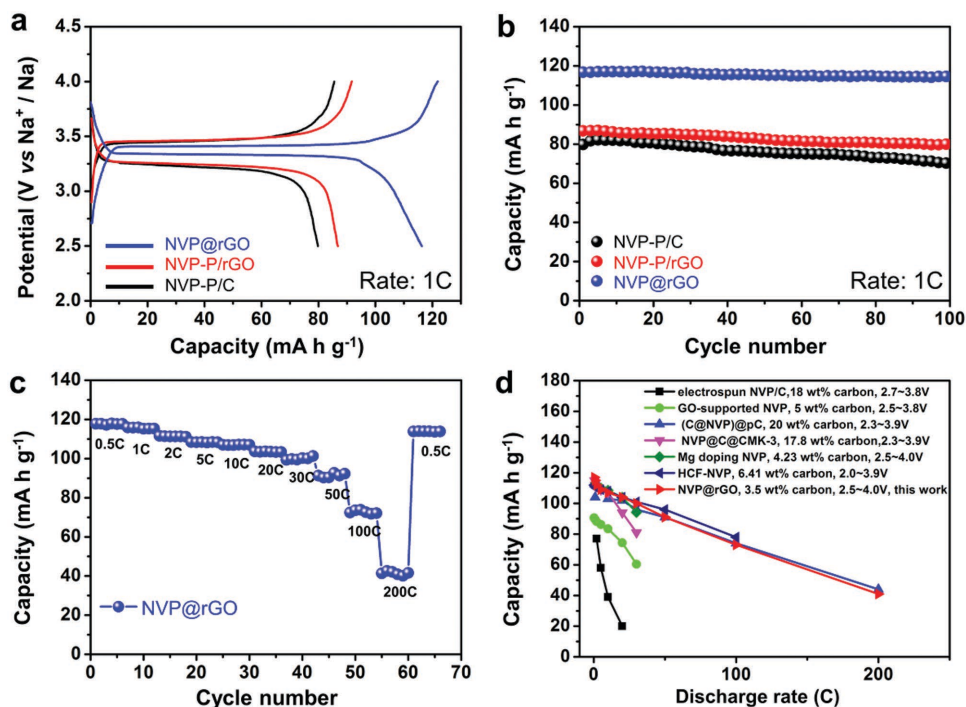
www.MaterialsViews.com

ADVANCED
ENERGY
MATERIALS
www.advenergymat.de

FULL PAPER

Figure 4. a) The initial charge–discharge curves of NVP-P/C, NVP-P/rGO, and NVP@rGO at 1 C. b) Cycling performance of NVP-P/C, NVP-P/rGO, and NVP@rGO at 1 C. c) Rate performance of the NVP@rGO and d) comparison of rate performance of NVP@rGO to the recent results in the literature for NVP (electrospun NVP/C,[54] GO-supported NVP,[48] (C@NVP)@pC,[38] NVP@C@CMK-3,[39] Mg doping NVP,[32] and HCF-NVP[40]).

and 100 C, respectively. At an even higher rate of 200 C, the NVP@rGO still delivers a substantial capacity of 41 mA h g^{-1}, where the charge/discharge process can be completed in 6.7 s. When the rate is turned back to 0.5 C, the reversible capacity can be recovered to 115 mA h g^{-1}, exhibiting remarkable rate recovery. Compared with those of NVP-P/C, NVP-P/rGO, and unlayered-NVP@rGO (Figure 4c and Figures S11c and S13, Supporting Information), the layered NVP@rGO composite exhibits remarkable enhanced rate performance at different rates (especially at high rates). The mass loading will affect the rate performance. When the mass loading is increased from 1.5–2.0 to 3.5–4.0 mg cm^{-2}, the NVP@rGO still shows excellent rate performance (Figure S14, Supporting Information): the discharge capacity of 115, 55, and 38 mA h g^{-1} at 1, 100, and 200 C, respectively. The results prove the well-design layered NVP@rGO with remarkable rate capability even under a high mass loading.

A comparison of the rate capabilities of the state-of-the-art NVP electrode reported in the literature is displayed in Figure 4d.[32,38–40,48,54] The specific comparison data is shown in Table S3 of the Supporting Information. To the best of our knowledge, our designed NVP@rGO delivers almost the same high-rate capacity compared to the best reported results but with lowest carbon contents (3.5 wt%) and relatively narrow voltage window (2.5–4.0 V).[38,40] In addition, the excellent rate capability of the NVP@rGO is even comparable to the high performance of LIBs cathodes.[36,37,55,56] The Ragone plots (energy density vs power density) of the samples are further displayed in Figure S15 of the Supporting Information. In terms of NVP@rGO, the energy density can be estimated to

be 387.8 Wh kg^{-1} with a power density of 0.21 kW kg^{-1}. More significantly, the energy density still retains 107.2 Wh kg^{-1} with a power density of 55.11 kW kg^{-1}. Such excellent result is significantly better than that of the current advanced cathodes, such as LiFePO$_4$/rGO,[55] Li(Ni$_{1/3}$Co$_{1/3}$Mn$_{1/3}$)O$_2$,[56] Na$_{0.6}$Fe$_{0.5}$Mn$_{0.5}$O$_2$,[19] Na$_4$Fe(CN)$_6$/C.[57] These results indicate that the as-prepared NVP@rGO cathode is a very promising candidate for the high power energy storage devices, even comparable to the supercapacitors but with higher energy density.

Figure 5a shows the cycling performance of the obtained three samples at a rate of 5 C. The NVP@rGO delivers a high initial specific capacity of 111 mA h g^{-1} and maintains a reversible capacity of 102 mA h g^{-1} after 500 cycles, corresponding to a capacity retention of 92%. However, for NVP-P/C and NVP-P/rGO, the reversible capacity is only 38 and 50 mA h g^{-1} after 500 cycles at 5 C, corresponding to the capacity retention of 55% and 62%, respectively. As for the unlayered-NVP@rGO, the initial capacity is about 101 mA h g^{-1}. After 400 cycles, the capacity maintains 87% (Figure S11d, Supporting Information). Compared with that of the layerd NVP@rGO, the result indicates that the freeze-drying process is important for obtaining the designed layered NVP@rGO structure, which largely enhanced the rate and cycling performance. Figure S16 of the Supporting Information shows the long-term cycling life of NVP@rGO for 1000 cycles at 10 C and the corresponding charge–discharge curves for selected cycles, respectively. The initial capacity is 110 mA h g^{-1} while a capacity of 99 mA h g^{-1} is left after 1000 cycles. In addition, representative charge–discharge curves and long-life cycling performance of NVP@rGO at high rate of 20 C are shown in Figure 5b,c. The NVP@rGO cathode exhibits an
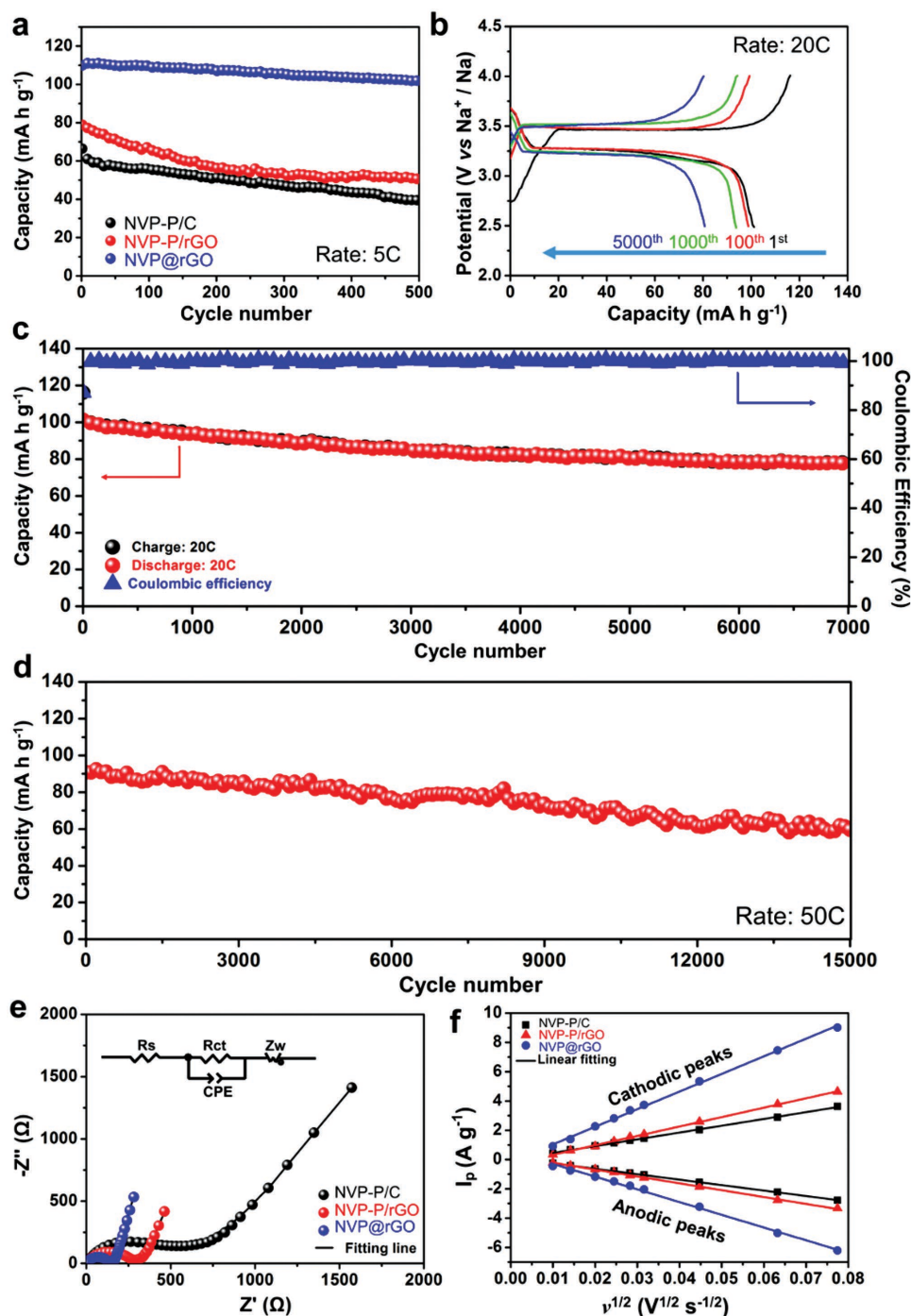
ADVANCED
ENERGY
MATERIALS
www.advenergymat.de

www.MaterialsViews.com

FULL PAPER

Figure 5. a) Cycling performance of NVP-P/C, NVP-P/rGO, and NVP@rGO cathodes at 5 C. b) Charge–discharge curves of the NVP@rGO at 20 C in different cycles. c) Cycling stability of the NVP@rGO for 7000 cycles at rate of 20 C. d) Ultralong cycling stability of the NVP@rGO for 15 000 cycles at a high rate of 50 C. e) The Nyquist plots of the NVP-P/C, NVP-P/rGO, and NVP@rGO after two cycles with equivalent circuit inset. f) Linear fitting of I_p versus $\nu^{1/2}$ curves from the redox peaks in CV curves.

initial discharge capacity of 101 mA h g^{-1}, and more than 78.0% capacity (79 mA h g^{-1}) is still remained after 7000 cycles. The Coulombic efficiency averages 99.7%, indicating that the electrochemical Na$^+$ insertion/extraction process is highly reversible. More significantly, ultralong-life cycling performance of NVP@rGO at high rate of 50 C is shown in Figure 5d.

The NVP@rGO not only delivers a high initial discharge capacity of 90 mA h g^{-1}, but also retains capacity of 63 mA h g^{-1} after 15 000 cycles, corresponding to the capacity retention of 70.0%. The capacity retentions of NVP@rGO after long-term cyclability at different rates are summarized in Table S4 of the Supporting Information. The cycling stability is also better

www.MaterialsViews.com

ADVANCED
ENERGY
MATERIALS

www.advenergymat.de

FULL PAPER

than the state-of-the-art reported NVP cathodes[2,13,18,32,38,39,48,54] and exceeds most other rechargeable sodium batteries significantly.[22–30] Moreover, the SEM images of NVP@rGO after 10 000 cycles at 50 C were shown in Figure S17a,b of the Supporting Information. Compared with the SEM images before cycling (Figure 3a,b), there is no apparent difference between before cycling and after 10 000 cycles, which indicates that the layer-by-layer stable structure is highly effective in promoting ultrafast electronic transport and assisting in buffering volume change of Na+ insertion/extraction.

The electrochemical impedance spectra (EIS) measurements on the assembled cells after two cycles for NVP-P/C, NVP-P/rGO, and NVP@rGO were investigated to reveal the reason for the enhanced electrochemical performance for the layer-by-layer structured nanocomposite. The Nyquist plots are shown in Figure 5e. The charge transfer resistance (R_{ct}) of both graphene modified products, NVP@rGO (130 Ω) and NVP-P/rGO (268 Ω), are much smaller than that of NVP-P/C (468 Ω), indicating that graphene modification improves the charge transfer kinetics. However, the R_{ct} of NVP@rGO is much smaller than that of NVP-P/rGO, demonstrating that the layer-by-layer assembly of NVP@rGO provides more efficient electron/ion transport than that of the NVP-P/rGO due to the uniform dispersion of rGO and well contact between NVP and rGO matrices.[58–60]

In order to further demonstrate the enhanced electrochemical performance for NVP@rGO composite, cyclic voltammetry (CV) was measured at different scan rates shown in Figure S18 of the Supporting Information. The NVP@rGO (Figure S18a, Supporting Information) maintains the well-defined redox peaks completely even at a high scan rate of 6 mV s−1 in the range of 2.5–4.0 V. The current of NVP@rGO is the highest among the three samples, indicating its highest reversibility and fastest kinetics during electrochemical reaction.[36,61] It is proposed that the peak current $I_p = a v^b$, here a is a constant and v is the scan rate. The b-value can change from 1/2 (semi-infinite diffusion) to 1 (capacitive processes).[62] From the fitting lines (Figure 5f), both the sodiation and desodiation currents exhibit a well linear relation with $v^{1/2}$, indicting a diffusion controlled process during the sodium storage in NVP. Therefore, the faster diffusion kinetics would lead to a higher rate performance. Based on Randles Sevcik equation (Equation (1)),[63] the Na-ion diffusion coefficient D (cm2 s−1) can be calculated from the linear relationship between peak currents I_p (A) and the square root of scan rates $v^{1/2}$:

$$I_p = 2.69 \times 10^5 n^{3/2} A D^{1/2} C v^{1/2} \tag{1}$$

where n is the number of electrons per molecule during the intercalation, A is the surface area of the cathode (cm2), C is the concentration of Na ions in the electrode (mol cm−3). The cathodic and anodic D of NVP@rGO are calculated to be 2.45×10^{-10} and 1.32×10^{-10} cm2 s−1, higher than those of NVP (5.01×10^{-12} and 3.24×10^{-12} cm2 s−1) and NVP-P/rGO (2.60×10^{-11} and 1.42×10^{-11} cm2 s−1), which evidently proves the fast charge transfer kinetics and thus the enhanced rate capability.

In the case of practical applications, the electrochemical performance of NVP at low and high temperature should be proposed. Here, to assess the performance of our synthesized NVP@rGO composite, we tested the electrochemical performance at a low temperature of 0 °C and a high temperature of 60 °C. **Figure 6**a shows the first charge–discharge curves of NVP@rGO at different temperatures in the potential ranges
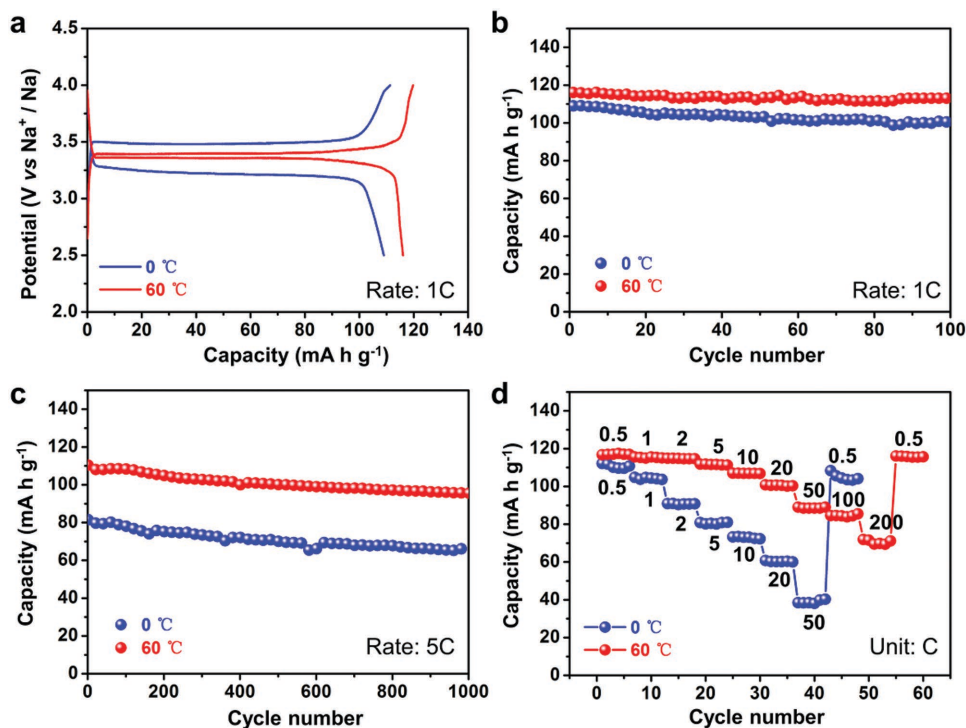

Figure 6. a) The initial charge–discharge curves at 1 C, b) cycling performance at 1 C, c) cycling performance at 5 C, and d) rate performance of NVP@rGO at 0 and 60 °C between 2.5 and 4.0 V.

ADVANCED
ENERGY
MATERIALS

www.advenergymat.de

FULL PAPER

www.MaterialsViews.com

of 2.5–4.0 V at 1 C. At high temperature (60 °C), the electrode exhibits high capacity of 117.1 mA h g^{-1} and a tiny overpotential (32 mV). At the operation temperature of 0 °C, the NVP@rGO delivers a relatively high overpotential (255 mV), which may be due to the increased charge-transfer resistance and slow ion kinetics at low temperature.[64] But, a high discharge capacity of 109 mA h g^{-1} is still obtained at such low temperature, owing to the rapid ion diffusion and electron transport rate of the NVP@rGO. After 100 cycles (Figure 6b), the capacity retention is 98.0% at 60 °C and 92.0% at 0 °C, respectively. Figure 6c shows the cycling performance of NVP@rGO at a rate of 5 C at different temperatures. The electrode delivers a high initial specific capacity of 112 mA h g^{1} at 60 °C and maintains a reversible capacity of 96 mA h g^{-1} after 1000 cycles, corresponding to a capacity retention of 87%. At 0 °C, the electrode still delivers an initial capacity of 82 mA h g^{-1}. Its capacity maintains 66 mA h g^{-1} after 1000 cycles, corresponding to the capacity retention of 80%. Figure 6d shows the rate performance of NVP@rGO at different temperatures. With the current rate is increased to 10, 50, and 100 C, the discharge capacities still remain 108, 90, and 85 mA h g^{-1}, respectively. Even up to 200 C, the NVP@rGO delivers a substantial capacity of 70 mA h g^{-1}, which is higher than the capacity obtained at room temperature. When the rate is turned back to 0.5 C, the reversible capacity can be recovered to 116 mA h g^{-1}, exhibiting remarkable rate recovery. At 0 °C, the electrode delivers a high discharge capacity of 112 mA h g^{-1} at 0.5 C. With the current rate is increased to 10, 20, and 50 C, the electrode can still delivers considerable capacity of 73, 61, and 40 mA h g^{-1}.

3. Conclusion

A novel layer-by-layer NVP@rGO composite is synthesized through modifying the surface charge of NVP gel precursor. Combining the advantages of NVP and rGO, the novel layer-by-layer structure offers high electronic and ionic conductivity, rapid Na$^+$ diffusion, and electron transport pathway, and stable structure during sodiation/desodiation, leading to the excellent rate capability and ultralong-life cycling stability. With very low carbon content (only ≈3.0 wt% rGO and 0.5 wt% amorphous carbon), this NVP@rGO cathode displays superior rate capability (91 mA h g^{-1} at 50 C, 73 mA h g^{-1} at 100 C, 41 mA h g^{-1} at 200 C) and ultralong cyclability (63 mA h g^{-1} at 50 C after 15 000 cycles). Moreover, the NVP@rGO nanocomposite still shows stable cycling performance and excellent rate capability at both low and high operating temperatures. Our work demonstrates that the novel layer-by-layer NVP@rGO is a very promising cathode for the high performance SIBs. We believe that this effective strategy can also be extended to other cathode or anode materials for advanced energy storage applications.

4. Experimental Section

Synthesis: Graphene oxide (GO) was prepared using the famous Hummers method as previously reported.[46,65] A stoichiometric ratio (1.5:2:3) of sodium carbonate (Na$_2$CO$_3$), vanadium (III) acetylacetonate (V(C$_5$H$_7$O$_2$)$_3$), and ammonium dihydrogen phosphate (NH$_4$H$_2$PO$_4$) were added in a beaker containing 40 mL deionized water. After ultrasonic treatment for 1 h, the solution was stirred overnight at room temperature in order to obtain a homogenous solution and then was transferred into a 50 mL Teflon-lined stainless steel autoclave and kept at 180 °C for 6 h, followed by natural cooling to room temperature. Subsequently, a green jelly-like NVP gel precursor was obtained. Then, 3 mL GO solution (3 mg mL^{-1}) was added into the gel precursor under vigorous stirring until get a stable dispersion, followed by a freeze-drying process. The product was grounded, then was annealed at 750 °C for 8 h with a heating rate of 2 °C min^{-1} in Ar/H$_2$ (95:5 in vol.) to finally obtain the NVP@rGO composite. As control experiments, the NVP-P/C was prepared through the same process without adding GO. The NVP-P/rGO composite was prepared without a pre-hydrothermal process. To investigate the effect of freeze-drying process, unlayered-NVP@rGO was prepared similar to that of NVP@rGO through replacing the freeze-drying treatment to a normal drying (70 °C in an oven).

Material Characterization: Zeta potential (Zetasizer 3000HS) was measured to characterize the effective surface charge of the samples. XRD (Burker D8 Advanced X-ray diffractometer with Cu-Kα radiation) was employed to characterize the structural properties of the samples. CHN elemental analyzer was involved in determining the carbon contents in the as-prepared samples. Raman spectra were obtained using a Renishaw INVIA micro-Raman spectroscopy system. SEM images were collected with a JEOL-7100F microscopy. TEM and HRTEM images were recorded by using a JEM-2100F STEM/EDS microscope.

Electrochemical Characterization: The electrochemical properties were evaluated by assembly of 2016 coin cells in a glove box filled with pure argon gas. The active electrode was made by putting the mixture of 70 wt% active material, 20 wt% carbon black, and 10 wt% PVDF with an appropriate amount of N-methyl-2-pyrrolidone (NMP) as a solvent on an Al foil. Then the working electrode was dried in a vacuum oven for 6 h at 100 °C. The mass loading is 1.5-2.0 mg cm^{-2}. In sodium half cells, sodium metal was used as the anode, a 1 M solution of NaClO$_4$ in ethylene carbonate (EC)/dimethyl carbonate (DMC) (EC:DMC = 1:1, w%) with 5% FEC was used as electrolyte, and glass fiber (GF/D) from Whatman was used as the separator. The galvanostatic charge–discharge tests were carried out at a voltage window of 2.5–4.0 V on a battery test system (LAND CT2001A). Cyclic voltammetry (CV) and AC-impedance spectra were tested with an electrochemical workstation (CHI 600e and Autolab PGSTAT 302N).

Supporting Information

Supporting Information is available from the Wiley Online Library or from the author.

Acknowledgements

[1] S. Chu, A. Majumdar, *Nature* **2012**, *488*, 294.
[2] S. Li, Y. Dong, L. Xu, X. Xu, L. He, L. Mai, *Adv. Mater.* **2014**, *26*, 3358.
[3] J. Liu, *Adv. Funct. Mater.* **2013**, *23*, 924.
[4] P. Yang, J. M. Tarascon, *Nat. Mater.* **2012**, *11*, 560.
[5] B. Dunn, J. M. Tarascon, *Science* **2011**, *334*, 928.
[6] M. Pasta, C. D. Wessells, R. A. Huggins, Y. Cui, *Nat. Commun.* **2012**, *3*, 704.
[7] L. Suo, Y. S. Hu, H. Li, M. Armand, L. Chen, *Nat. Commun.* **2013**, *4*, 66.
[8] J. B. Goodenough, K. S. Park, *J. Am. Chem. Soc.* **2013**, *135*, 1167.
[9] L. Mai, Q. Wei, Q. An, X. Tian, Y. Zhao, X. Xu, L. Xu, L. Chang, Q. Zhang, *Adv. Mater.* **2013**, *25*, 2969.
[10] Y. Ding, Y. Wen, C. Wu, P. A. van Aken, J Maier, Y. Yu, *Nano Lett.* **2015**, *15*, 1388.
[11] C. Zhu, X. Mu, P. A. van Aken, J. Maier, Y. Yu, *Adv. Energy Mater.* **2014**, *5*, 9.
[12] B. L. Ellis, W. R. Makahnouk, Y. Makimura, K. Toghill, L. F. Nazar, *Nat. Mater.* **2007**, *6*, 749.
[13] Z. Jian, W. Han, X. Lu, H. Yang, Y. S. Hu, J. Zhou, Z. Zhou, J. Li, W. Chen, D. Chen, *Adv. Energy Mater.* **2013**, *3*, 156.
[14] V. Palomares, P. Serras, I. Villaluenga, K. B. Hueso, J. Carretero-González, T. Rojo, *Energy Environ. Sci.* **2012**, *5*, 5884.
[15] L. Wang, Y. Lu, J. Liu, M. Xu, J. Cheng, D. Zhang, J. B. Goodenough, *Angew. Chem. Int. Ed.* **2013**, *52*, 1964.
[16] N. Recham, J. N. Chotard, L. Dupont, K. Djellab, M. Armand, J. M. Tarascon, *J. Electrochem. Soc.* **2009**, *156*, A993.
[17] M. D. Slater, D. Kim, E. Lee, C. S. Johnson, *Adv. Funct. Mater.* **2013**, *23*, 947.
[18] K. Saravanan, C. W. Mason, A. Rudola, K. H. Wong, P. Balaya, *Adv. Energy Mater.* **2013**, *3*, 444.
[19] N. Yabuuchi, M. Kajiyama, J. Iwatate, H. Nishikawa, S. Hitomi, R. Okuyama, R. Usui, Y. Yamada, S. Komaba, *Nat. Mater.* **2012**, *11*, 512.
[20] C. Yuliang, X. Lifen, W. Wei, C. Daiwon, N. Zimin, Y. Jianguo, L. V. Saraf, Y. Zhenguo, L. Jun, *Adv. Mater.* **2011**, *23*, 3155.
[21] R. Berthelot, D. Carlier, C. Delmas, *Nat. Mater.* **2011**, *10*, 74.
[22] S. Komaba, T. Nakayama, A. Ogata, T. Shimizu, C. Takei, S. Takada, A. Hokura, I. Nakai, *ECS Trans.* **2009**, *16*, 43.
[23] D. Su, G. Wang, *ACS Nano* **2013**, *7*, 11218.
[24] S. Tepavcevic, H. Xiong, V. R. Stamenkovic, X. Zuo, M. Balasubramanian, V. B. Prakapenka, C. S. Johnson, T. Rajh, *ACS Nano* **2011**, *6*, 530.
[25] Q. Wei, J. Liu, W. Feng, J. Sheng, X. Tian, L. He, Q. An, L. Mai, *J. Mater. Chem. A* **2015**, *3*, 8070.
[26] Y. Kawabe, N. Yabuuchi, M. Kajiyama, N. Fukuhara, T. Inamasu, R. Okuyama, I. Nakai, S. Komaba, *Electrochem. Commun.* **2011**, *13*, 1225.
[27] K. T. Lee, T. N. Ramesh, F. Nan, G. Botton, L. F. Nazar, *Chem. Mater.* **2011**, *42*, 3593.
[28] R. A. Shakoor, D. H. Seo, H. Kim, Y. U. Park, J. Kim, S. W. Kim, H. Gwon, S. Lee, K. Kang, *J. Mater. Chem.* **2012**, *38*, 20535.
[29] F. Sauvage, E. Quarez, J. M. Tarascon, E. Baudrin, *Solid State Sci.* **2006**, *8*, 1215.
[30] C. Wu, P. Kopold, Y. L. Ding, P. A. V. Aken, J. Maier, Y. Yu, *ACS Nano* **2015**, *9*, 6610.
[31] Z. Jian, V. Raju, Z. Li, Z. Xing, Y. S. Hu, X. Ji, *Adv. Funct. Mater.* **2015**, *25*, 5778.
[32] H. Li, X. Yu, Y. Bai, F. Wu, C. Wu, L. Y. Liu, X. Q. Yang, *J. Mater. Chem. A* **2015**, *3*, 9578.
[33] X. Rui, W. Sun, C. Wu, Y. Yu, Q. Yan, *Adv. Mater.* **2015**, *27*, 6670.
[34] D. Kundu, E. Talaie, V. Duffort, L. F. Nazar, *Angew. Chem. Int. Ed.* **2015**, *54*, 3431.
[35] J. Kang, S. Baek, V. Mathew, J. Gim, J. Song, H. Park, E. Chae, A. K. Rai, J. Kim, *J. Mater. Chem.* **2012**, *22*, 20857.
[36] Q. Wei, Q. An, D. Chen, L. Mai, S. Chen, Y. Zhao, K. M. Hercule, L. Xu, A. Minhas-Khan, Q. Zhang, *Nano Lett.* **2014**, *14*, 1042.
[37] Y. Luo, X. Xu, Y. Zhang, Y. Pi, Y. Zhao, X. Tian, Q. An, Q. Wei, L. Mai, *Adv. Energy Mater.* **2014**, *4*, 1400107.
[38] C. Zhu, K. Song, P. A. van Aken, J. Maier, Y. Yu, *Nano Lett.* **2014**, *14*, 2175.
[39] Y. Jiang, Z. Yang, W. Li, L. Zeng, F. Pan, M. Wang, X. Wei, G. Hu, L. Gu, Y. Yu, *Adv. Energy Mater.* **2015**, *5*, 1402104.
[40] Y. Fang, L. Xiao, X. Ai, Y. Cao, H. Yang, *Adv. Mater.* **2015**, *27*, 5895.
[41] W. Li, Z. Liang, Z. Lu, H. Yao, W. S. Zhi, K. Yan, G. Zheng, Y. Cui, *Adv. Energy Mater.* **2015**, *5*, 1500211.
[42] X. Rui, Q. Yan, M. Skyllas-Kazacos, T. M. Lim, *J. Power Sources* **2014**, *258*, 19.
[43] X. Yang, C. Cheng, Y. Wang, L. Qiu, D. Li, *Science* **2013**, *341*, 534.
[44] A. K. Geim, *Science* **2009**, *324*, 1530.
[45] M. J. Allen, V. C. Tung, R. B. Kaner, *Chem. Rev.* **2009**, *110*, 132.
[46] Y. Sun, Q. Wu, G. Shi, *Energy Environ. Sci.* **2011**, *4*, 1113.
[47] D. Chen, H. Feng, J. Li, *Chem. Rev.* **2012**, *112*, 6027.
[48] Y. H. Jung, C. H. Lim, D. K. Kim, *J. Mater. Chem. A* **2013**, *1*, 11350.
[49] R. J. Hunter, *Foundations of Colloid Science*, 2nd ed., Oxford University Press Inc, New York **2001**, p. 376.
[50] B. Konkena, S. Vasudevan, *J. Phys. Chem. Lett.* **2012**, *3*, 867.
[51] W. Duan, Z. Hu, K. Zhang, F. Cheng, Z. Tao, J. Chen, *Nanoscale* **2013**, *5*, 6485.
[52] Q. Li, Q. Wei, J. Sheng, M. Yan, L. Zhou, W. Luo, R. Sun, L. Mai, *Adv. Sci.* **2015**, *2*, 1500284.
[53] S. Helveg, C. Lopez-Cartes, J. Sehested, P. L. Hansen, B. S. Clausen, J. R. Rostrup-Nielsen, F. Abild-Pedersen, J. K. Nørskov, *Nature* **2004**, *427*, 426.
[54] J. Liu, K. Tang, K. Song, P. A. van Aken, Y. Yu, J. Maier, *Nanoscale* **2014**, *6*, 5081.
[55] X. Zhu, J. Hu, W. Wu, W. Zeng, H. Dai, Y. Du, Z. Liu, L. Li, H. Ji, Y. Zhu, *J. Mater. Chem. A* **2014**, *2*, 7812.
[56] M. Oljaca, B. Blizanac, A. Du Pasquier, Y. Sun, R. Bontchev, A. Suszko, R. Wall, K. Koehlert, *J. Power Sources* **2014**, *248*, 729.
[57] J. Qian, M. Zhou, Y. Cao, X. Ai, H. Yang, *Adv. Energy Mater.* **2012**, *2*, 410.
[58] B. Li, N. Zhang, K. Sun, *Small* **2014**, *10*, 2039.
[59] H. Zhang, H. Tao, J. Yong, J. Zheng, M. Wu, Z. Bing, *J. Power Sources* **2010**, *195*, 2950.
[60] W. Guoxiu, L. Hao, L. Jian, Q. Shizhang, L. G. Max, M. Paul, A. Hyojun, *Adv. Mater.* **2010**, *22*, 4944.
[61] J. Su, X. L. Wu, J. S. Lee, J. Kim, Y. G. Guo, *J. Mater. Chem. A* **2013**, *1*, 2508.
[62] G. A. Muller, J. B. Cook, H.-S. Kim, S. H. Tolbert, B. Dunn, *Nano Lett.* **2015**, *15*, 1911.
[63] W. Hao, Y. Li, C. Huang, Y. Zhong, S. Liu, *J. Power Sources* **2012**, *208*, 282.
[64] Y. Qiao, J. Tu, X. Wang, C. Gu, *J. Power Sources* **2012**, *199*, 287.
[65] R. Offeman, W. Hummers, *J. Am. Chem. Soc.* **1958**, *80*, 1339.